

Galactic Distribution of Supernovae and OB Associations

M. Kachelrieß and V. Mikalsen

Institutt for fysikk, NTNU, Trondheim, Norway

Abstract

We update and extend a previous model by Higdon and Lingenfelter for the longitudinal profile of the N II intensity in the Galactic plane. The model is based on four logarithmic spiral arms, to which features like the Local Arm and local sources are added. Connecting then the N II to the H II emission, we use this model to determine the average spatial distribution of OB associations in the Milky Way. Combined with a stellar mass and cluster distribution function, the model predicts the average spatial and temporal distribution of core-collapse supernovae in the Milky Way. In addition to this average population, we account for supernovae from observed OB associations, providing thereby a more accurate description of the nearby Galaxy. The complete model is made publicly available in the python code **SNOB**.

Keywords: OB associations, core-collapse supernovae, cosmic ray sources, N II line intensity, structure of the Milky Way

PROGRAM SUMMARY

Manuscript Title: Galactic Distribution of Supernovae and OB Associations

Program Title: SNOB 1.1: Simulating the distribution of SuperNovae and OB associations in the Milky Way

Journal Reference:

Catalogue identifier:

Licensing provisions: CC by NC 3.0.

Programming language: Python 3.8

Computer: Any computer with python version 3 installed

Operating system: Any system with python version 3

RAM: Depends on the parameter `num_grad_subdivision`

Keywords: OB associations, core-collapse supernovae, cosmic ray sources, N II line intensity

Solution method: Numerical integration of line-of-sight integrals for the N II line intensity; Monte Carlo simulation of the spatial and time distribution of OB associations and core-collapse supernovae.

Contents

1	Introduction	2
2	Modelling the N II intensity of the Galactic plane	3
2.1	FIRAS data and fitting procedure	3
2.2	Axial-symmetric model	4
2.3	Spiral arm model	6
2.3.1	Four-arm model	6
2.3.2	Cygnus region	8
2.3.3	Gum Nebula	8
2.3.4	Local Arm	8
2.3.5	Devoid region of the Sagittarius-Carina Arm	9
2.3.6	Summary	9
3	Supernova progenitor distribution	10
3.1	Connecting OB associations and supernovae	10
3.1.1	SNe per associations	10
3.1.2	Individual SNe	12
3.2	Known OB associations	12
3.3	Comparison with observational data	12
4	Program structure	15
4.1	observational_data	16
4.2	nii_intensities	16
4.3	galaxy_model	18
5	Summary	18

1. Introduction

The mechanical energy injected by supernovae (SNe) explosions into the interstellar medium (ISM) has been a prime candidate to power the acceleration of Galactic cosmic rays (CR) since the first suggestion by Baade and Zwicky [1–3]. In addition, these explosions generate the Galactic populations of stellar black holes and pulsars, are the main source of heavier elements up to the iron group, and drive the turbulence of the ISM. Thus SNe are key factors for the evolution and dynamics of galaxies, and therefore of high interest. Around 80%–90% of all SN explosions are core-collapse SNe, marking the end of stellar fusion in stars with initial mass above $\simeq 8 M_{\odot}$ [4, 5]. Therefore, the progenitors of these stars are of the OB type, which are the main emitters of ionizing radiation in the Milky Way. Moreover, the life-time of these massive stars is short, and thus core-collapse SNe should happen close to their birthplace in associations of OB stars.

An important ingredient in simulations of CR propagation and the prediction of the primary and secondary CR fluxes is the source distribution of CR sources. The details of the CRs source distribution become more important for those CRs whose propagation distance in the Galaxy is short: Important examples are electrons in the TeV energy range and above because of their severe energy losses, and CR protons close to PeV energies because of their fast escape from the Galaxy. For instance, it has been argued that a significant change in the observed positron flux at Earth is caused by the spiral structure of the Milky Way [6]. Moreover, the interpretation of the fluxes of radioactive cosmic ray isotopes is significantly affected how the effect of the Milky Way spiral arms is included [7]. In practise, however, most often the CR source distribution is modelled using a template based on the distribution of pulsars. Since pulsars are normally not observed soon after their birth and receive rather large kick velocities at birth, their spatial distribution does not resolve the spiral structure of the Milky Way. Moreover, the rather large errors and the small number of their distance estimates allows only the determination of their radial distribution [8–10].

As an alternative, Higdon and Lingenfelter suggested to use the distribution of OB associations as a proxy for the distribution Galactic CR sources [11, 12]. The use of such a proxy is well justified for a rather generic class of CR sources, including SN remnants, young pulsars, pulsar wind nebula, and superbubbles or a combination of these source types. Moreover, the position of OB associations can be traced by the observation of their line emission, choosing e.g. the H II line. It is, however, more convenient to use instead the N II emission line, as in this case absorption can be neglected. In particular, Higdon and Lingenfelter suggested to use the lateral distribution of the N II 205 μ m line intensity observed by the FIRAS instrument on-board the COBE satellite. In order to construct the three-dimensional distribution of OB associations from the two-dimensional sky picture of the N II 205 μ m intensity, a model for the spatial structure of the Milky Way has to be supplemented which then can be fitted to the observational data.

The aim of the present work is to provide a simulation tool which generates the spatial and temporal distribution of core-collapse supernovae in the Milky Way. In this work, we follow closely the approach of Higdon and Lingenfelter [11, 12]. Compared to their analysis, we update several parameters like the Solar distance to the Galactic center, which requires a re-fitting of the model parameters. More importantly, we add new elements like the Local Arm and a devoid region of the Sagittarius-Carina Arm, as well as using information on observed nearby OB associations. The resulting model can be used for reproducing the N II intensity in the Galactic plane, and for simulating OB associations and past SNe in the Milky Way. In addition to the use of H II regions as source distribution for Galactic CRs, pulsars or black holes, accounting for H II regions might be useful in the interpretation of radio dispersion and scattering measurements as electron density tracers [13]. The complete model is made publicly available¹ in the python code `SNOB`.

2. Modelling the N II intensity of the Galactic plane

Our aim in this section is to reproduce the N II 205 μ m intensity measured in the Galactic plane by the FIRAS instrument on-board the COBE satellite [14]. After a brief discussion of the data and our fitting procedure, we first introduce an axial-symmetric three-dimensional model which will then serve as the foundation for a more realistic source model based on spiral arms.

2.1. FIRAS data and fitting procedure

We want to use the longitudinal profile of the N II intensity in the Galactic plane as shown in Fig. 5(e) of Ref. [14] to calibrate our source model for the Galactic N II emission. For a given spatial distribution of the isotropic N II line emissivity $\varepsilon(\mathbf{x})$ in the Milky Way, the intensity I in the direction specified by the Galactic longitude l and latitude b can be calculated from the line-of-sight integral

$$I(l, b) = \frac{1}{4\pi} \int_0^{r_{\max}} dr \varepsilon(r, l, b). \quad (1)$$

Here, r denotes the distance from the Sun, while r_{\max} is the maximal distance of Galactic N II sources. Moreover, we use that absorption can be neglected for this line.

The FIRAS beam approximately was a top hat with an opening angle of 7°, and thus the instrument was not able to resolve the Galactic plane. As a simple alternative to the procedure used in Ref. [14] to derive the intensity $I(l, b = 0)$ in the Galactic plane, we use the following recipe suggested by Fixsen [15]: We average our modelled intensities over $\Delta l = 5^\circ$ in latitude, while we integrate them over $b = \pm 5^\circ$ in longitude. Then we divide by $\Delta b = 1^\circ$, assuming that all radiation from the Galactic plane is contained within $|b| < 0.5^\circ$. Thus we compare the average intensities $\langle I(l, 0) \rangle$ of our models in the Galactic plane defined by

$$\langle I(l, 0) \rangle = \frac{1}{\Delta l \Delta b} \int_{b=-5^\circ}^{b=+5^\circ} db \cos b \int_{l=-2.5^\circ}^{l=+2.5^\circ} dl \int_0^{r_{\max}} dr \frac{\varepsilon(r, l, b)}{4\pi} \quad (2)$$

¹To be released after acceptance of this article.

to the longitudinal profile $I(l, 0)$ of the FIRAS data shown in Ref. [14]. In order to fit the parameters of the source models, we employ a χ^2 test,

$$\chi^2 = \frac{1}{N - m} \sum_{i=1}^N \frac{(O_i - C_i)^2}{\sigma_i^2}. \quad (3)$$

Here, C_i are the modelled and O_i the observed intensities, respectively, while σ_i is the error of the observed intensity C_i . In the final version of the model, the number of fit parameters amounts to $m = 40$ while the number of data points is $N = 1800$. This large number of parameters makes the testing of all different combinations unpractical. Instead, the parameters used in Ref. [12] were taken as a starting point and adjusted first by eye until the model became reasonable as compared to the FIRAS data. Then subsets of parameters were fitted within a chosen range around their initial value.

Even though the final model has 40 parameters, it remains relatively simple compared to the complexity of the Milky Way, and thus there are several regions where the model severely over- or underestimates the N II intensities. As the deviations of the model from the observed data are so prominent at specific bins, the algorithm for optimising the parameters would favour parameters which minimise these large deviations at the expense of other features of the spiral arms. Examples of this behaviour are the skewing of the Sagittarius-Carina Arm to minimise the gap at $l = 280^\circ$ at the expense of its spiral arm tangents, and favouring a significant fractional contribution for Norma-Cygnus at the expense of Perseus to minimise the gap at $l = 330^\circ$ and $l = 350^\circ$. From observations, it is known that Perseus and Scutum-Crux are the most luminous arms, rendering the latter solution incompatible with observations. Therefore, several bins were removed from the calculation of the reduced χ^2 during the optimisation of the parameters to keep the model reasonable compared to observations. These were the bins at $l = \{5^\circ, 45^\circ, 275^\circ, 280^\circ, 330^\circ, 335^\circ, 350^\circ\}$ which are highlighted in Fig. 1. However, the reduced χ^2 values given below are calculated from all the data points—thus the listed bins were only left out for the fitting process.

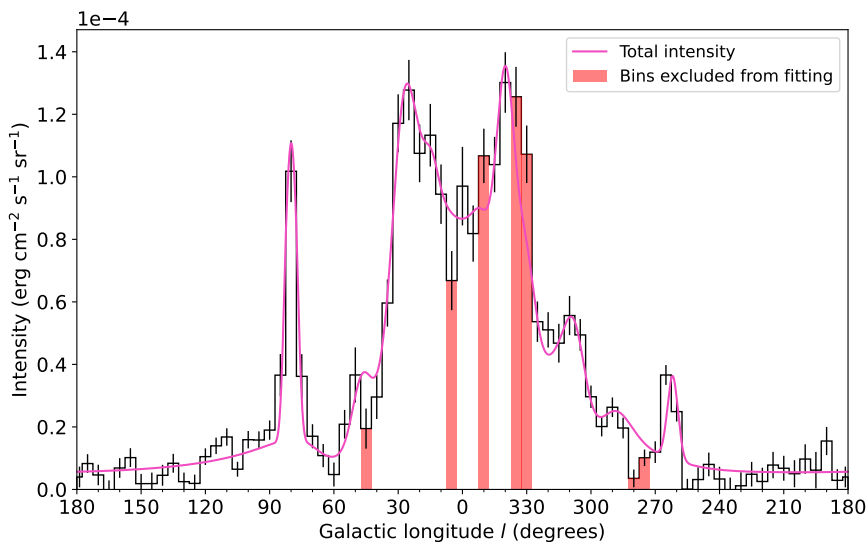


Figure 1: N II $205\mu\text{m}$ line intensity (magenta line) in the Galactic plane for the best-fit model as function of the Galactic longitude together with the measured N II line intensity (black histogram) from FIRAS in Figure 5(e) of [14]; the bins removed from the fitting procedure are highlighted in red.

2.2. Axial-symmetric model

The simplest approach to model the Galactic N II emissivity is to approximate the distribution of sources in the Milky Way as a cylinder and to assume axial symmetry. To convert from Galactic to Galactocentric

cylindrical coordinates, we use

$$\rho = \sqrt{x^2 + y^2} = \sqrt{r^2 \cos^2 b + R_\odot^2 - 2R_\odot r \cos b \cos l}, \quad (4a)$$

$$\vartheta = \arctan(y/x) = \arctan\left(\frac{R_\odot - r \cos b \cos l}{r \cos b \sin l}\right), \quad (4b)$$

$$z = r \sin b, \quad (4c)$$

with $R_\odot = 8.2$ kpc as the Solar distance to the Galactic center, as suggested by the results of the GRAVITY Collaboration [16]. In addition to axial symmetry, we assume that the radial and the vertical dependence of the N II $205\mu\text{m}$ line emissivity factorise, such that we can set

$$\varepsilon(\rho, z) = LS(\rho)P(z)/A. \quad (5)$$

Here, L is the total Galactic N II $205\mu\text{m}$ luminosity, $S(\rho)$ is the (dimensionless) radial and $P(z)$ the (dimensionfull) vertical dependence of the N II source distribution, while A denotes the effective Galactic disk area. For the vertical distribution $P(z)$ of N II sources we employ following Ref. [12] a Gaussian distribution,

$$P(z) = \frac{e^{-z^2/2\sigma_z^2}}{\sqrt{2\pi}\sigma_z}. \quad (6)$$

Because of the large beam size of the FIRAS instrument, the FIRAS data cannot be used to determine the width σ_z of this distribution. Instead, one can use hydrogen radio recombination lines (RRL) as a tracer for the distribution of H II regions, which are known to stem from their outer envelopes [17, 18]. Reference [18] showed that the low-frequency RRL have a full width at half maximum (FWHM) of about 1.8° in latitude. They also found that 75% of the identified H II regions in high-frequency RRL surveys were located in the Galactic plane, with $|b| < 1.5^\circ$. Moreover, a more recent study [19] of RRLs in 106 Galactic H II regions found only four regions with a Galactic latitude greater than 4° , while 88 were within $|b| < 1^\circ$, equating to about 74% of the sample size. These studies substantiate the argument that H II regions are strongly concentrated in the Galactic disk. Reference [12] estimated that $\sigma_z = 0.15$ kpc reproduces the FWHM reported by [18]. Even though this value is much greater than the exponential scale height of OB stars of 0.045 pc [20] and the scale height of molecular clouds of 0.035 kpc [21], it is comparable to the estimate in Ref. [22], where $\sigma_z = 0.15$ kpc as value for the vertical scale height σ_z of H II regions is reported. This is the value we adopt also in this work.

For the (dimensionless) radial distribution $S(\rho)$ of N II sources we employ following Ref. [22] an exponential distribution,

$$S(\rho) \propto e^{-\rho/H_\rho^{\text{N II}}}, \quad (7)$$

for $\rho_{\min} \leq \rho \leq \rho_{\max}$. We use $\rho_{\min} = 3$ kpc and $\rho_{\max} = 11$ kpc, corresponding to the boundary of the H II regions listed in Ref. [23]. In order to determine the scale length $H_\rho^{\text{N II}}$, we have to account for the radial N/H gradient which biases the radial N II and H II distributions. Assuming for all three distributions an exponential dependence, $\propto \exp(-\rho/H_i)$ with scale length $H_i = \{H^{\text{H II}}, H^{\text{N II}}, H^{\text{N/H}}\}$, they are connected by

$$\frac{1}{H_\rho^{\text{N II}}} \simeq \frac{1}{H_\rho^{\text{N/H}}} + \frac{1}{H_\rho^{\text{H II}}}. \quad (8)$$

Reference [24] recently revisited the radial abundance gradients of nitrogen and oxygen. They selected 13 H II regions located at Galactocentric distances between 5.7 kpc and 16.1 kpc. Because of their low degree of ionisation, the authors of Ref. [24] argued that their number for the nitrogen radial abundance gradient is the first which is independent of the ionisation correction factor. Their reported change is -0.059 ± 0.009 dex/kpc. Inserting $10^{0.059} \simeq 1.15$ per kpc together with $H_\rho^{\text{H II}} = 3.5$ kpc from Ref. [22] into Eq. (8), we obtain $H_\rho^{\text{N II}} = 2.4$ kpc. Finally, the effective Galactic disk area A is defined as the disk area weighted by the disk emissivity,

$$A = \int d\vartheta \int d\rho \rho S(\rho) = 2\pi (H_\rho^{\text{N II}})^2 [(1 + \rho_{\min}/H_\rho)S(\rho_{\min}) - (1 + \rho_{\max}/H_\rho)S(\rho_{\max})], \quad (9)$$

which with the adopted values for ρ_{\min} , ρ_{\max} and H_{ρ}^{NII} evaluates to $A = 21.265 \text{ kpc}^2$.

Following Ref. [12], this axial-symmetric model is then normalised to the observed FIRAS NII intensity at the longitude $l = 30^\circ$. Our best-fit model shown in Fig. 2 together with the observed intensities from Ref. [14] requires a total Galactic NII luminosity of $1.9 \times 10^{40} \text{ erg/s}$, which is in close agreement with the value $1.8 \times 10^{40} \text{ erg/s}$ obtained by Higdon and Lingenfelter. From the figure, it is clear that this model poorly reproduces the observed intensities outside the Galactic center region, as it falls off too slowly and fails to capture many of the structures visible in the data. Hence, a more complicated and accurate model is needed and will be constructed next.

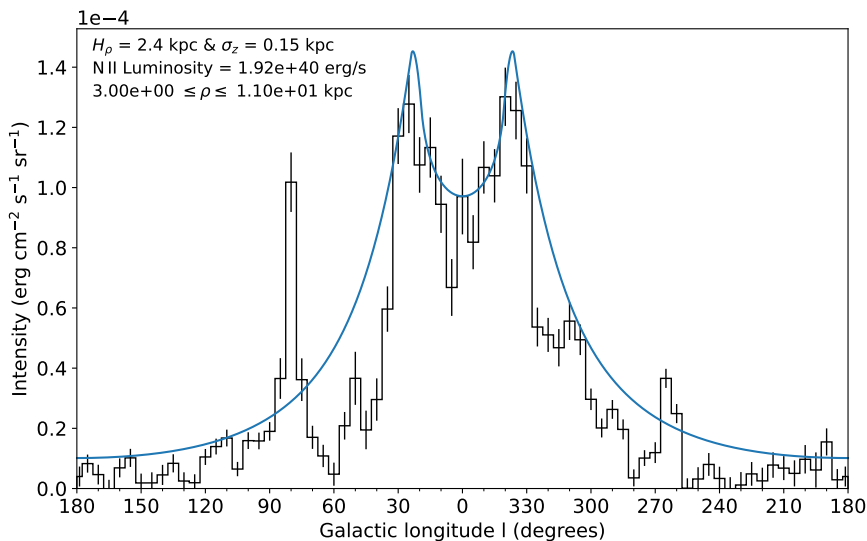


Figure 2: N II $205\mu\text{m}$ line intensity (blue line) as function of the Galactic longitude in the axial-symmetric model together with the measured NII line intensity (black histogram) from FIRAS in Figure 5(e) of [14].

2.3. Spiral arm model

We consider next a model with four spiral arms, adding then the Cygnus region and the Gum nebula which are clearly visible local H II regions. Moreover, we introduce the Local Arm and an underdense region in the Sagittarius-Carina Arm.

2.3.1. Four-arm model

Studying H II regions and their massive ionising stars, Ref. [25] proposed that the Galaxy consists of four spiral arms known as Norma-Cygnus (NC), Perseus (P), Sagittarius-Carina (SA), and Scutum-Crux (SC), for more recent works on the spiral arm structure of the Milky Way see Refs. [26–28]. Both Refs. [26] and [28] use a logarithmic model for the positions $\rho(\vartheta)$ of the spiral arm medians in the Galactocentric cylindrical coordinate system, where $\rho(\vartheta) = \rho_{\min} e^{k(\vartheta - \vartheta_0)}$ for $\rho_{\min} \leq \rho \leq \rho_{\max}$ with $k = \tan(p)$. Here, p is the pitch angle for the given spiral arm, ρ_{\min} and ρ_{\max} are respectively the inner and outer limits of the spiral arm, and ϑ_0 is the starting angle for the spiral arm as measured counter-clockwise from the x axis. Following Refs. [12, 26, 29], we will use $\rho_{\min} = 2.9 \text{ kpc}$ and $\rho_{\max} = 35 \text{ kpc}$ for the inner and outer limit of the spirals. Since we use the more up-to-date value of $R_{\odot} = 8.2 \text{ kpc}$, the starting angles and pitch angles have been refitted from the FIRAS data. The obtained values are listed in Tab. 1 in units of degrees. The resulting four-arm spiral model is shown in the left panel of Fig. 3 together with the Local Arm, which will be discussed later.

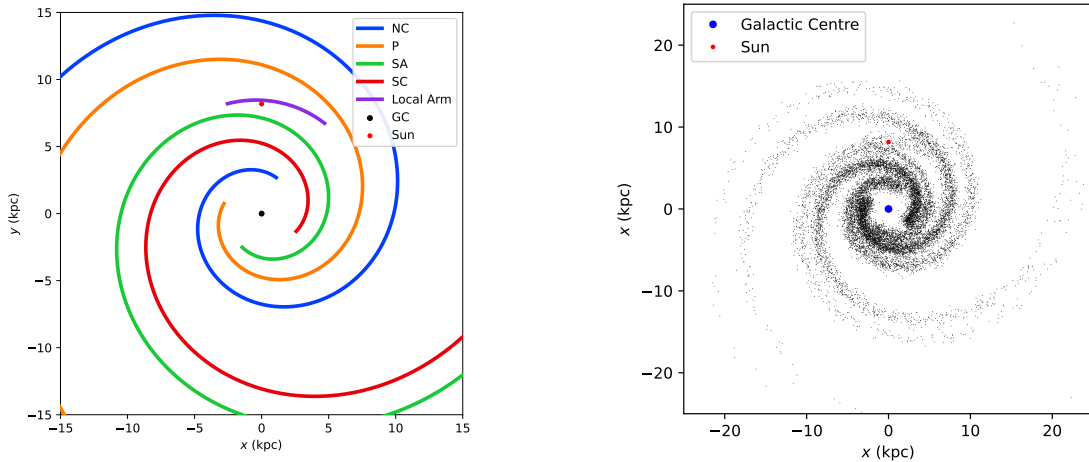


Figure 3: Left: Schematic view of the Milky Way, showing the four major spiral arms Norma-Cygnus (NC), Perseus (P), Sagittarius-Carina (SA), and Scutum-Crux (SC), as well as the Local Arm. The Galactic center (GC) and the Sun are also shown. Right: Modelled Galaxy after 100 Myrs. Each black dot represents an OB association with at least 2 OB stars.

	$\vartheta_{0,NC}$	$\vartheta_{0,P}$	$\vartheta_{0,SA}$	$\vartheta_{0,SC}$	p_{NC}	p_P	p_{SA}	p_{SC}	f_{NC}	f_P	f_{SA}	f_{SC}
our fit	68	165	240	333	13.5	15.1	13.8	16.2	0.19	0.35	0.16	0.29
Ref. [12]	70	160	250	340	13.5	13.5	13.5	15.5	0.18	0.36	0.18	0.28

Table 1: The starting and pitch angles in degrees, plus the relative weight of the four spiral arms from our fit to the FIRAS data compared to the values of Ref. [12].

Following Refs. [30, 31], the width of the arms is modelled by a Gaussian,

$$P_{\Delta}(\Delta) = e^{-\Delta^2/2\sigma_{\Delta}^2}. \quad (10)$$

Note that the transverse densities P_{Δ} are normalised to one at $\Delta = 0$ such that they give the relative density with respect to the arm median density, which is given by

$$P_{\rho}(\rho) = e^{-\rho/H_{\rho}}. \quad (11)$$

In addition, Eq. (10) is used to determine the fall-off in density at the end of the spiral arms, where the calculated densities are projected on a circular arc of 180° around the final point. This ensures a smooth transition at the endpoint to the surrounding medium. As in the axial-symmetric model of section 2.2, the distribution vertical to the Galactic plane is given by Eq. (6) with $\sigma_z = 0.15$ kpc. The relative planar density of each spiral arm is given by the product $P_{\rho}(\rho)P_{\Delta}(\Delta)$. The source-weighted area of the spiral arm i becomes

$$A_i = \int_0^{2\pi} d\vartheta \int_0^{r_{\max}} d\rho \rho P_{\rho}(\rho_j(\rho, \vartheta)) P_{\Delta}(\Delta), \quad (12)$$

where ρ_j is a given point along the spiral arm median as a function of ρ and ϑ . The function P_{Δ} remains the same for each spiral arm and every ρ_j , as the transverse density always is relative to the arm median density.

Finally, each of the four spiral arms is given a relative weight f_i to reproduce the observational data more accurately. This is in line with, e.g., Ref. [32] who fitted a three-dimensional model of the far-infrared (FIR) and near-infrared (NIR) data measured by COBE/DIRBE and found that the spiral arms Scutum-Crux and Perseus dominated the NIR emission. To improve their model, they had to reduce the Sagittarius-Carina Arm's luminosity relative to the other arms. Other works such as Refs. [33–35] also support that the

Name	$\vartheta_{0, \text{LA}}$	$\vartheta_{\text{max, LA}}$	p_{LA}	f_{LA}
Hou & Han	55.1	110	2.77	
our fit	55.1	107	2.77	0.01

Table 2: Starting and maximal angle, and the relative weight of the Local Arm, from our fit compared to those of Ref. [28].

Sagittarius-Carina arm is weaker than the other arms. Reference [29] also finds that the Scutum-Crux and Perseus arms have significantly stronger emissions than the Sagittarius-Carina and Norma-Cygnus arms. As for the spiral arm angles and pitch angles, the values given by [12] have to be tweaked to fit with the new parameters for the Galaxy, and the obtained values can be found in Table 1. Note that the sum of all fractional contributions only adds to 0.99. This is because we anticipate the inclusion of the Local Arm, which will be described in subsection 2.3.4.

2.3.2. Cygnus region

The Cygnus region is a massive star forming region of our Galaxy, containing several OB associations and hundreds of OB stars [36, 37]. The most massive of these associations is the well-known Cyg OB2 association, which contains at least 50 O stars. Cyg OB2 is embedded in the large star forming region called Cygnus X located at $l \simeq 80^\circ$, $b \simeq 0.8^\circ$ [37–39], with an angular extension of $\simeq 10^\circ$ [40]. The bright feature in the FIRAS data at $l \simeq 80^\circ$ will thus be interpreted as the star forming region Cygnus X. Following Ref. [12], this feature is modelled as a uniform sphere located at $(l, b) = (80^\circ, 0^\circ)$ with a radius of $R = 75$ pc, corresponding to an angular width of $\simeq 12^\circ$. To mimic the effect of the 7° FIRAS beam, the modelled intensities from Cygnus X were weighted with a Gaussian distribution with a full width at half maximum of 7° . In the same manner as for the spiral arm intensities, the contribution from the Cygnus X region was averaged over $\Delta l = 5^\circ$ and $\Delta b \simeq 5.9^\circ$, with Δb being the angular extent of the source. The fitted N II luminosity for Cygnus X is 2×10^{37} erg/s, identical to the value obtained in Ref. [12].

2.3.3. Gum Nebula

The bright feature in the FIRAS data at $l \simeq 260^\circ$ is interpreted as the H II region known as the Gum Nebula, first reported in Ref. [41]. This H II region is primarily excited by the massive runaway O4I star ζ Puppis and the binary γ^2 Velorum in the Vela OB2 association, the latter being composed of a massive O star and a Wolf-Rayet star [42]. The most massive and brightest member of Vela OB2 is γ^2 Velorum which is located at $l = 262.8^\circ$, $b = -7.7^\circ$ [43] at a distance of 368_{-13}^{+38} pc [44]. Following Ref. [12], the feature in the FIRAS data at $l \simeq 260^\circ$ is modelled as a single spherical source located at $l = 262^\circ$, $b = 0^\circ$ and a distance of 330 pc. As for Cygnus X, the Gum Nebula will be weighted over a normal distribution with a full width at half maximum of 7° to simulate the effect of the FIRAS beam. It will also be averaged over $\Delta l = 5^\circ$ and $\Delta b \simeq 10.4^\circ$. The required N II luminosity of the Gum Nebula is 1.2×10^{36} erg/s, which is consistent with the value obtained in Ref. [12]. The effect of including Cygnus X and the Gum Nebula to the N II intensity profile can be seen in Fig. 4.

2.3.4. Local Arm

In addition to the four major arms, star forming regions between the Perseus and Sagittarius-Carina Arms have been known for a long time. Reference [28] recently investigated the spiral structure of the Milky Way, employing data from more than 2500 known H II regions, 1300 giant molecular clouds (GMCs), and 900 6.7 GHz methanol masers. They found that a model with four major spiral arms and a Local Arm best fitted the data. The Local Arm begins near the Perseus Arm and extends past the Sun towards the Sagittarius-Carina Arm. The parameters from Ref. [28] for the Local Arm together with a value for the fractional contribution and the result from the reduced χ^2 fitting are given in Table 2. We use the values for $\vartheta_{0, \text{LA}}$ and p_{LA} given in Ref. [28], while $\vartheta_{\text{max, LA}}$ and f_{LA} were fitted.

The result of adding the Local Arm to the model can be seen in Fig. 5. The most notable contribution to the resulting N II line intensity are the regions $l \simeq 70^\circ$ and $l \simeq 110^\circ$. The inclusion of the Local Arm also contributes towards the Gum Nebula, increasing the total modelled N II intensities to match the observed

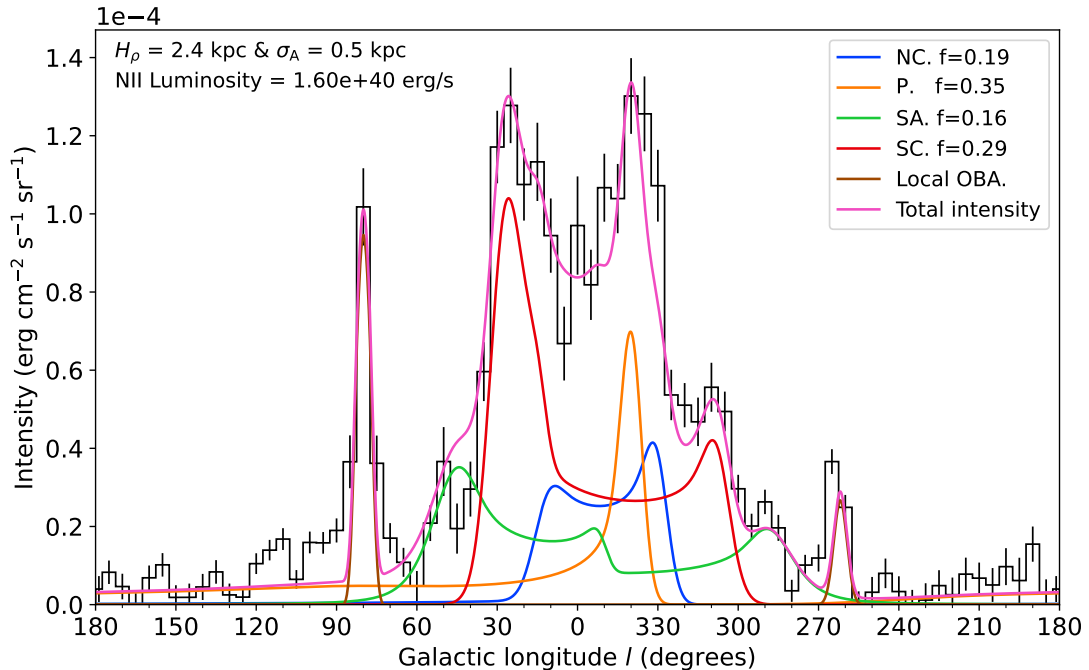


Figure 4: N II line intensity for the four spiral arm model plus the Cygnus X and the Gum nebula. The measured N II line from FIRAS in Figure 5(e) of [14] is shown as a histogram.

data. The inclusion of the Local Arm lowered the reduced χ^2 from 16.72 to 12.47. Contrary to Ref. [12], we thus conclude that including the Local Arm improves the model considerably.

2.3.5. Devoid region of the Sagittarius-Carina Arm

Looking at Fig. 5, it is clear that the model is overestimating the intensities in the range $l = 20^\circ$ to $l = 65^\circ$. This portion of the Sagittarius-Carina Arm has been known for a long time to be devoid of optical tracers and to suffer from heavy extinction [45–47]. We select a specific portion of the arm in this direction to model this devoid region, reducing the corresponding σ_d . This effectively leads to a faster fall-off of the density surrounding to the arm median, instead of simply decreasing the modelled densities of the entire arm segment. As shown in Fig. 6, the resulting Sagittarius-Carina Arm matches the observed intensities in this region better. The devoid region is defined by the parameters $\rho_{\min} = 5.1$ kpc, $\rho_{\max} = 7.0$ kpc and $\sigma_d = 0.25$ kpc, where ρ_{\min} determines the closest distance from the Galactic center to the devoid region and ρ_{\max} the other edge further away from the Galactic centre. After incorporating the devoid region, the overall fit for the model improves, lowering the reduced χ^2 from 12.47 to 11.25.

2.3.6. Summary

Our final model for the N II emissivity consists of the seven components described above: Four logarithmic spiral arms with individual weights, where we include in the case of the Sagittarius-Carina Arm an underdense region, plus the Local Arm. In addition, the Cygnus region and the Gum nebula as the two most important local H II regions were taken into account. The N II intensity of these individual contributions and the resulting total intensity is shown in Fig. 6.

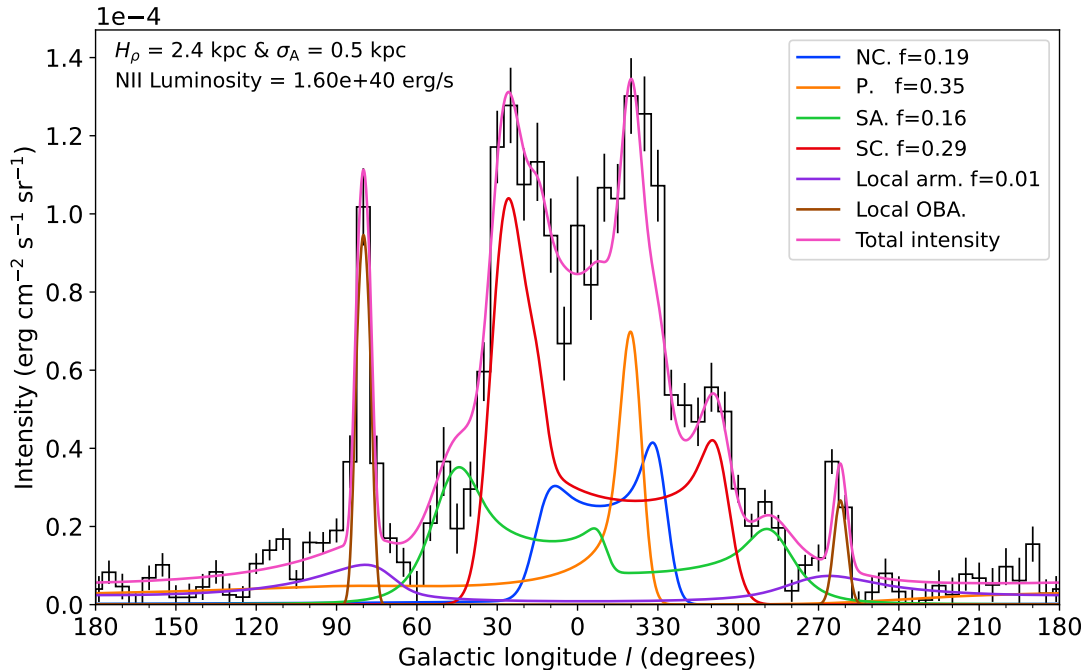


Figure 5: N II line intensity for the four spiral arm model adding two local sources and the Local Arm. The measured N II line from FIRAS in Figure 5(e) of [14] is shown as a histogram.

3. Supernova progenitor distribution

The model for the Galactic N II emission developed in the previous section will be the basis for the spatial probability distribution of OB associations and SNe in the Milky Way. In order to make the model in our local neighbourhood more accurate, we add those observed OB associations where we have reliable information on their distance, mass and age.

3.1. Connecting OB associations and supernovae

3.1.1. SNe per associations

The number of newly born associations and their stellar content should reflect the expected SNe birthrate, which is about three per century [48, 49], out of which about 80%–90% are core-collapse SNe of type II and Ib/c. How the mass of the OB association is distributed among different stars is determined by the stellar initial mass function (IMF). We will here use the modified Kroupa IMF, where the index α_3 has been increased from 2.35 to 2.7 to take into account unresolved binaries [50]. Combining then the size-frequency distribution of young stellar clusters, the modified Kroupa IMF and the study of ionising luminosities in Ref. [22], the number of clusters born per Myr with a number of stars N_* between N_* and $N_* + dN_*$ was derived in Ref. [11] as

$$\frac{dn_{\text{sc}}(N_*)}{dN_* dt} = 1.65 \left(\frac{1.7 \times 10^6}{N_*^{1+\alpha}} \right) / \text{Myr}, \text{ for } 190 \leq N_* \leq 1.7 \times 10^6. \quad (13)$$

Here, $n_{\text{sc}}(N_*)$ is the number of clusters with N_* stars of all masses. The slope α of this power law has to be determined from observations of H II regions: The authors of Ref. [51] investigated 30 nearby galaxies and found as best fit value $\alpha = 1 \pm 0.5$, while Ref. [22] obtained $\alpha = 0.99 \pm 0.25$ focusing on OB associations in the Milky Way and excluding the smallest H II regions due to incompleteness in the dataset on the lower end.

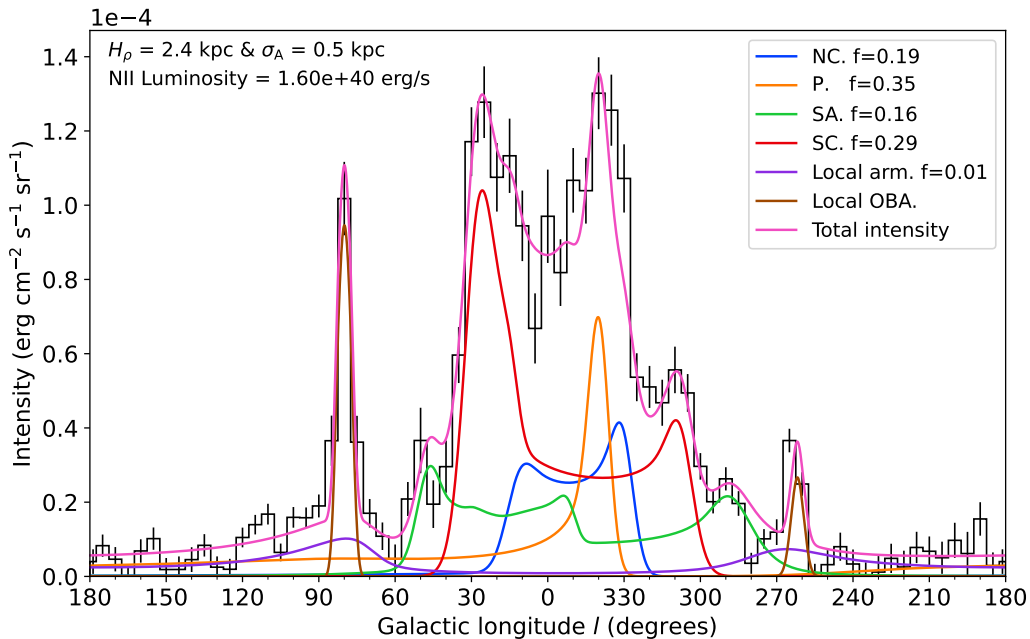


Figure 6: NII intensity for the four spiral arm model adding two local sources, the Local Arm and the devoid region of Sagittarius. The measured NII line from FIRAS in Figure 5(e) of [14] is shown as a histogram.

A value close to one is also theoretically expected, because otherwise massive stars would be concentrated either in the smallest or largest associations. We will use as our default parameter $\alpha = 0.8$, a value within the reported uncertainties which fits better to the observational data on OB associations than $\alpha = 1$, as we will see later.

On average, the number of SN progenitors (SNPs) born is related to the total number of stars formed. Denoting by f_{SN} the fraction of formed stars with initial mass above $8 M_{\odot}$, which is the commonly stated minimum mass for core-collapse SNe [4, 5], the modified Kroupa IMF gives $f_{\text{SN}} = 1.1 \times 10^{-3}$ [11]. The expected number of SNPs to be born within an OB association follows from the cluster distribution in Eq. (13) multiplying the distribution by $f_{\text{SN}} N_*$ and integrating over the desired range. In total, the predicted birthrate of SNe is $2.81 \times 10^4/\text{Myr}$, or about one every 36 years—consistent with the expected number of Galactic SNe [52]. The cumulative probability distribution $P(> N_*^{\text{SN}})$ describes how the SNPs are distributed among the OB associations. In the case of g episodes of star formation in an association, it is given by

$$P(> N_*^{\text{SN}}) = C(g) - 0.11 \ln N_*^{\text{SN}}, \quad 1 < N_*^{\text{SN}} \leq 1870g, \quad (14)$$

where $C(g) = 0.828, 0.95$ and 1.0 for $g = 1, 3$ and 5 , respectively. The expected number of SNPs to be born in all Galactic OB association per Myr is 23270, 26600 and 28100 for $g = \{1, 3, 5\}$. For five such episodes, this model predicts that all of the OB stars in our Galaxy would be born in OB associations.

For $g = 1, 3$ and 5 , the upper limit for the number of massive stars in OB association becomes, respectively, 1870, 5610 and 9350. How does this fit with observations and models made by other authors? Reference [22] investigated SNPs with a minimum mass of $8 M_{\odot}$ and found for their model that the largest associations with five star forming episodes contained about 7200 OB stars. This is less than what the distribution of Ref. [11] predicts, but Ref. [22] did use a different IMF. Reference [22] compares their result with that of Refs. [53] and [54], and writes that their numbers correspond to, respectively, a maximum number of SNPs in Galactic associations of about 9000 and 7230. Thus, the upper limit for our model of 9350 SNPs in an association is on the higher end of this range.

In the right panel of Fig. 3, we show a Monte Carlo realisation of the Milky Way for a simulation time of 100 Myrs and five star formation episodes per OB association. Each black dot represents an OB association, containing at least 2 OB stars. The different relative weights of the four main arms as well as the Local Arm and the devoid region of Sagittarius-Carina are visible.

3.1.2. Individual SNe

When the number of SNPs to be born in OB associations per Myr is specified, a Monte Carlo simulation is used to draw associations from the distribution in Eq. (13) with limits given by $N_{\min}^{\text{SN}} = 2$ and $N_{\max}^{\text{SN}} = 1870$. Each association is populated g times from Eq. (13), and each star forming episode in an association is separated by 4 Myr [12, 22]. Reference [22] suggests that each star forming episode in an association results in roughly an equal number of stars, which agrees with the earlier work of [55]. Therefore, we will take the separate episodes of stars formation to contain an equal number of stars in our model. Once the associations and their stellar content are drawn, they are placed in the modelled Galaxy following the probability distribution of Galactic OB associations.

Then the masses for the OB stars are drawn randomly from the modified Kroupa IMF. The mass is then used to determine the lifetime of the star. Reference [56] investigated stellar evolutionary models and also gave data for the lifetimes of stars as a function of mass. These data were then used in Ref. [57] to fit the main-sequence lifetime in the mass range $2 \leq m/M_{\odot} \leq 67$. To make the function better fit the expected lifetimes for stars with even higher masses given in Ref. [56], we have scaled the function of [57] by a factor of 1.65:

$$\tau = 1.65\tau_0(M/M_{\odot})^{-\alpha}, \quad \tau_0 = 160 \text{ Myr}, \quad \alpha = 0.932. \quad (15)$$

The massive OB stars have now been assigned a mass, lifetime and birthplace in the Galaxy, with the birthplace being the association's center. These stars are not taken as stationary but will move about as time passes. Typically, the velocity dispersion within an OB association is of the order of a few km/s and anisotropic [37]. For simplicity, we assume a Gaussian isotropic velocity distribution with a dispersion of $\sigma = 2 \text{ km/s}$.

3.2. Known OB associations

We have compiled relevant data and information on observed OB associations mainly from the review [37]. We have added data² including the position, age, and the total mass of an association in stars with mass $M \geq M_{\min}$ found in Refs. [59, 60]. Using then the Kroupa IMF, the number of stars with mass larger than M_{\min} is derived and shown in Table 3.

3.3. Comparison with observational data

We now combine the modelled and observed associations into one unified model. The resulting plot of the Galaxy can be seen in Fig. 7. Here, the spiral arms are shown in the background with labels and the same colours as used in Fig. 5. The modelled associations are shown with green circles and the known ones in blue. The procedure for combining the modelled and known associations will next be described.

First, we generate a realisation of the Milky Way starting 100 Myr ago with five star forming episodes for each association and using the data on the known associations in Table 3. To populate the Galaxy with associations, we first add the known associations. Then concentric circles with a spacing of 0.5 kpc centred on the Sun are generated, which are also shown in Fig. 7. For each circular region, we compare the number of known associations to the number of modelled associations. If the number of known associations is less than the number of modelled associations, we randomly draw from the modelled associations located in this circular region until the sum of associations in this circular region equals the total number of modelled associations. Beyond 2.5 kpc, there are only modelled associations.

As seen from Fig. 7, this combined model follows the spirals arms, and the devoid region of Sagittarius-Carina is also visible. This figure explains also why we chose $\alpha = 0.8$ in Eq. (13) instead of $\alpha = 1$ as in

²For more details see Ref. [58].

Name	l /degree	b /degree	d /pc	t /Myr	N_s	M_{\min}/M_{\odot}	SNP	SNe	\leq Myr
Sco-Cen US	351.50	20.00	143	10	107	1.06	3	0	0
Sco-Cen UCL	331.00	12.50	136	16	179	1.06	6	1	0
Sco-Cen LCC	298.50	5.50	115	15	147	1.06	5	1	0
Ori OB1a	201.0	-17.3	360	12	234	2.0	22	2	0
Ori OB1b	205.0	-18.0	400	6	123	2.0	12	0	0
Ori OB1c	211.3	-19.5	385	4	246	2.0	23	0	0
Ori OB1d	209.0	-19.5	380	1	62	2.0	6	0	0
Vela OB2	262.80	-7.70	400	13	72	2.5	10	1	0
Trumpler 10	262.80	0.70	372	45	22	2.68	4	4	0
Cyg A	72.61	2.06	1895	14	125	2.68	20	3	0
Cyg B	78.58	3.31	1726	9	93	2.68	15	1	0
Cyg C	76.11	0.54	1713	8	88	2.68	14	1	0
Cyg D	75.44	1.19	2000	20	86	2.68	14	4	0
Cyg E	80.19	0.85	1674	8	133	2.68	21	1	0
Cyg F	74.04	1.44	1985	11	156	2.68	24	2	0
Cyg OB7	89.00	0.00	630	13	7	20	100	13	2
Aur 1	170.72	-0.16	1056	21	206	2.68	33	11	1
Aur 3	170.70	0.11	1514	12	111	2.68	17	2	0
Aur 4	173.09	-0.03	1923	2	128	2.68	20	0	0
Ara OB1	337.68	-0.92	1100	2	11	20	54	0	0
Per OB2	159.20	-17.10	318	10	9	2.68	1	0	0
Car OB1	286.50	-0.50	2350	6	294	2.68	45	1	0
CMa OB1	224.00	-1.30	1200	10	93	2.68	15	1	0
Mon OB1	202.10	1.00	700	5	24	2.68	4	0	0
Mon OB2	207.35	-1.60	1500	5	13	20	69	1	1
Sco OB1	343.30	1.20	1580	6	28	20	157	2	2
Lac OB1	96.70	-17.60	358	10	14	4.7	6	1	0
Sct OB2	23.18	-0.54	1170	6	14	2.68	2	0	0
Ser OB2	18.21	1.63	1900	5	107	2.68	17	0	0
Ser OB1	16.72	0.07	1706	5	20	20	106	2	1

Table 3: Observational data on known associations (position (l, b, d), age t and the number of stars N_s with mass $M > M_{\min}$) together with estimated past stellar content (total number of SNP, the number of past SNe, and the number of SNe in the last 1 Myr).

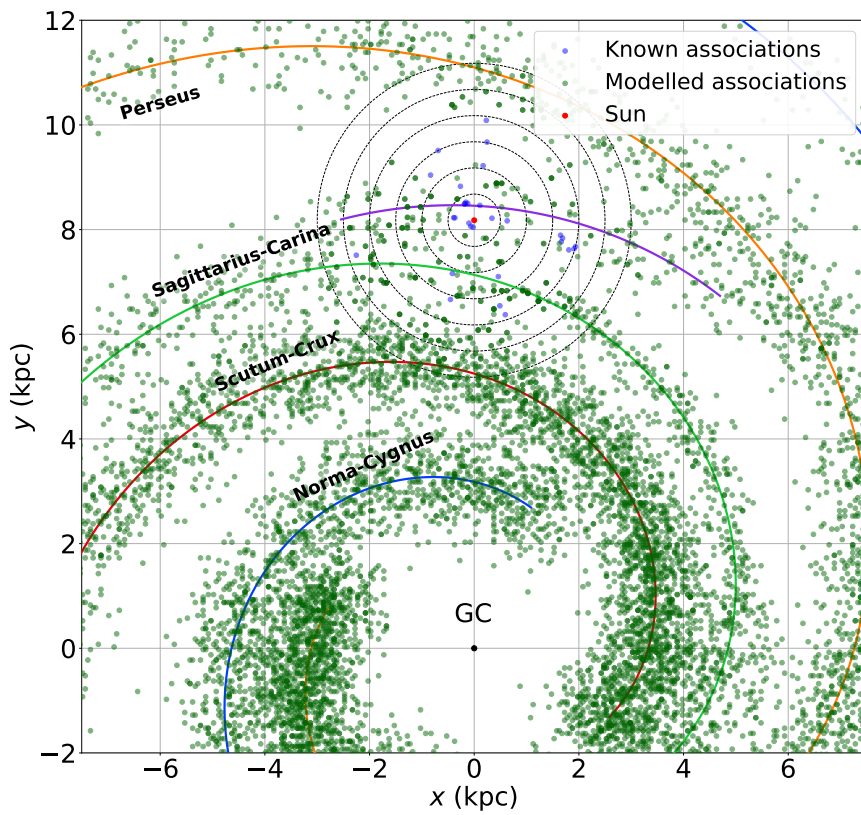


Figure 7: Distribution of OB associations after 100 Myr with five star formation episodes. Blue and green dots represent the known and modelled associations, respectively. The four major spiral arms and the Local Arm passing close to the Sun are highlighted.

Ref. [11]: One expects that, if not all, we should have observed the majority of the closest associations to Earth. Thus, there should be at most only a few modelled associations in the first circle in Fig. 7, what we achieve with $\alpha = 0.8$. A higher value for α makes the distribution in Eq. (13) steeper, meaning we would have many more associations with fewer stars, creating an over-abundance of modelled associations close to Earth.

In order to assess how accurate our model for the OB associations is, we first estimate the past stellar content of the known OB associations. To do this, we draw stars from the IMF until the number of surviving stars agrees with observed number of stars in the given mass range. In the last three columns of Table 3, we give the average number for the total number of stars with masses above $8 M_{\odot}$ after 10,000 iterations of this procedure. We have also given the number of past SNe that this procedure predicts and how many SNPs are left. Note that Trumpler 10 is estimated as having no stars left massive enough to produce a SN due to its old age. Finally, we compare the predictions for the mass distribution of stars in modelled to the one in observed OB associations, excluding the contribution of stars with mass $< 8 M_{\odot}$. In Fig. 8, we compare these two distributions using a bin width of $50 M_{\odot}$ and five episodes of star formation for the modelled associations. The exact count in each bin varies for each run, but overall, the fit between the mass distribution for modelled and known associations is good. With fewer episodes of star formation, the mass distribution for the modelled associations gets skewed towards the lower mass end, and thus, five episodes of star formation results in the best fit.

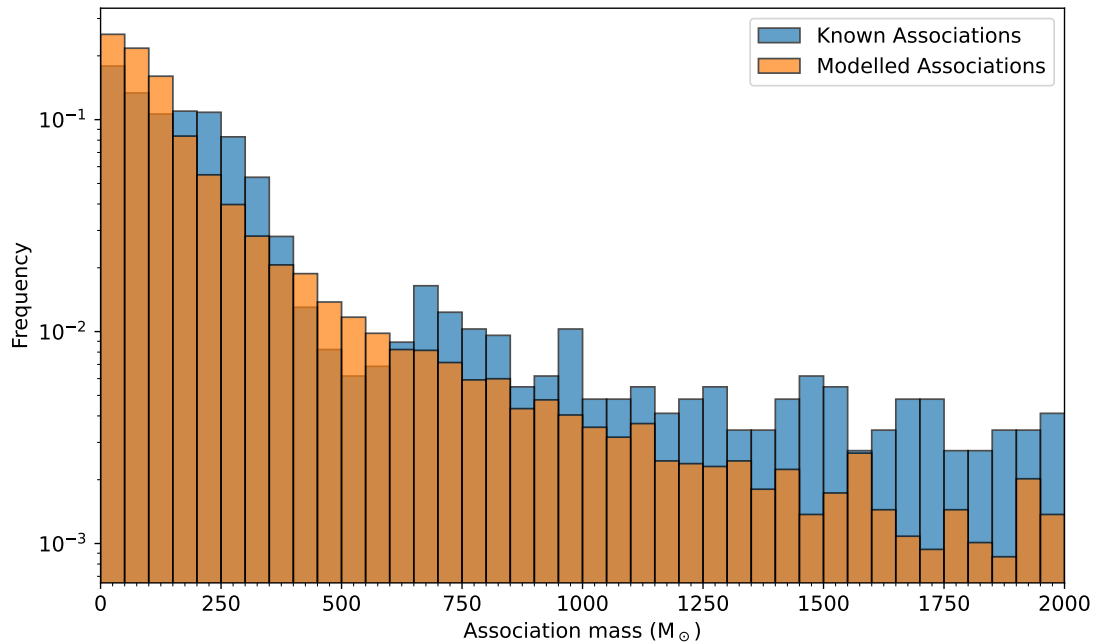


Figure 8: An example of the mass distribution of OB associations for five star forming episodes over 100 Myr compared to the one of known OB associations.

4. Program structure

The program has been written in `Python` and has been tested on both Linux and Windows. The code is distributed into five main folders: `galaxy_model`, `nii_intensities`, `tests`, `observational_data`, and `utilities`. Most of the figures in this article have been generated by the scripts in `tests`.

The code generating the Galaxy generates a rather large amount of data, and the data are therefore written to a file to save RAM. The code automatically checks if the folders for storing data and figures exist and generates them if they are missing, for instance, when running the code for the first time.

In the folder `utilities`, the user will find the files `constants.py` and `settings.py`. All parameters for the models are stored within `constants.py`, and the user can change, for instance, the scale-lengths `h_lyc`, `h_spiral_arm` and `h_axisymmetric`, and the distance between the Earth and Galactic center, `r_s`. Start angles, pitch angles, and maximum and minimum distance from the Galactic center for the four major spiral arms, the Local Arm and the devoid region of the Sagittarius-Carina Arm, are also defined within this file. The parameters for the broken power-law for the IMF, and τ and α which enters Eq. (15), are also found here, and the relative paths to where data and figures are stored are defined at the bottom of this file.

Within `settings.py`, four variables are defined: `num_grid_subdivisions`, `add_local_arm`, `add_devoid_region_sagittarius` and `add_gum_cygnus`. The three latter booleans determine whether or not if the Local Arm, the Sagittarius-Carina Arm’s devoid region, and the Cygnus X and the Gum Nebula shall be added to the model. These three booleans are by default set to `True`. `add_gum_cygnus` only affects whether or not Cygnus X and Gum Nebula shall be included in the NII intensity plot for the spiral arm model, as these regions already are taken into account from the known data when modelling OB associations.

The parameter `num_grid_subdivisions` splits up the interpolation procedure into smaller pieces, with `num_grid_subdivisions` being the number of pieces. The interpolation procedure is rather memory intensive due to the large amount of data generated, so to reduce memory needs, the user can split this workload into several smaller parts. Note that the larger the value for `num_grid_subdivisions`, the more time is required for the interpolation to finish. We recommend using `num_grid_subdivisions = 1` for 32 GB RAM and `num_grid_subdivisions = 4` for 8 GB RAM.

`utilities.py` contains various miscellaneous functions used in the calculations. Equation (4) is implemented via the functions `rho(r, l, b)`, `theta(r, l, b)` and `z(r, b)`, and converts the Earth-centric coordinates (r, l, b) to Galactocentric coordinates (ρ, ϑ, z) . The function `xy_to_long(x, y)` takes as input the x and y coordinates and calculates the corresponding longitude l . The function `axisymmetric_disk_population(rho, h)`, with `rho` being the distance from the Galactic center and `h` the scale-length of the Galactic disk, is the implementation of Eq. (7). Equation (6) is implemented in the function `height_distribution(z, sigma)`, with `z` being the vertical height from the Galactic plane and `sigma` determining the falloff in density transverse the plane.

For averaging the NII intensities for the longitudinal profiles, we have defined in `utilities.py` the function `running_average(data, window_size)`. `data` are the intensities, and `window_size` determines the number of points to calculate the average from for each value of l . The IMF and the stellar lifetime as a function of initial mass are also defined here.

4.1. *observational_data*

This folder contains programs handling the observational data. For instance, histograms of HII regions can be generated in `rrl_hii.py` by accessing the VizieR database. Part of the data entering Table 3 is calculated in `analysis_obs_data.py`, and in `firas_data.py` the FIRAS data, which were downloaded from NASA’s Goddard Space Flight Center, https://lambda.gsfc.nasa.gov/product/cobe/firas_prod_table.html, are prepared for plotting.

4.2. *nii_intensities*

In this folder, the axisymmetric and spiral arm models are generated by `axisymmetric_disk_model.py` and `spiral_arm_model.py`. Cygnus X and Gum Nebula are generated in `gum_cygnus.py`, and in `chi_squared.py` is a script optimising the parameters for the spiral arm model.

In `axisymmetric_disk_model.py`, we have two functions: `plot_axisymmetric()` and `calc_modelled_intensity(b_max = 5)`, where the former is responsible for loading the generated data and plotting it. The result is shown in Fig. 2. For `calc_modelled_intensity(b_max = 5)` there is one input parameter, namely `b_max` whose default value is 5° . This is the maximum angle in latitude for which we integrate over such that $\Delta b = 2b_{\text{max}}$. This is useful for testing how different limits for

the integration over latitude affect the resulting intensity plot. The other parameters entering the model, such as `rho_max_axisymmetric`, can be changed within `constants.py`. The resulting intensities for the axisymmetric model are saved to a `.numpy` file.

In `spiral_arm_model.py`, the function `calc_modelled_intensity()` calculates the spiral arm intensities. This function has the following eleven input parameters:

- `readfile_effective_area=True`: This boolean value controls whether or not the effective area per spiral arm shall be calculated. If it is set to `True` the values will be read from file, and if it is set to `False` the effective areas will be calculated and saved to file. It should be set to `False` when the code is run for the first time and whenever parameters for the spiral arms are changed, as this will affect the resulting effective areas.
- `interpolate_all_arms=True`: This boolean controls whether or not the densities for each arm shall be interpolated. If set to `True`, each spiral arm is interpolated over the entire Galactic plane, and then saved to file. The default value is set to `True`, as it is assumed the user will call the function `calc_modelled_intensity` only when spiral arm parameters are changed and thus need to recalculate the intensities. The reason for having this boolean in the first place is due to how the script for optimising the spiral arm parameters in `chi_squared.py` is designed. In short, we change the parameters for one arm at a time while keeping the others the same, and thus, we interpolate only one arm at a time. As such, we avoid interpolating the other arms multiple times for the same parameters, saving time. The intensities still need to be calculated, so we call `calc_modelled_intensity` with `interpolate_all_arms=False`. It should be set to `True` for all other uses.
- `calc_gum_cyg=False`: This boolean controls whether or not the modelled NII intensities from Cygnus X and Gum Nebula should be calculated. If set to `True`, the values will be calculated and saved to file by the script in `gum_cygnus.py`. It should be set to `True` the first time the script is run, and each time parameters for either Cygnus X or Gum Nebula are changed. Otherwise, it should be set to `False` to save time.
- `recalculate_coordinates=False`: The fourth and final boolean for this function controls whether or not the Galaxy coordinates should be recalculated. This process is time-consuming and should only be set to `True` the first time the script is run or if parameters for the Galaxy are changed, such as the maximum extent for the spiral arm `rho_max`, which is located in `constants.py`.
- `b_max=5` and `db_above_1_deg=0.2`: These parameters define the integration range over latitude and the step-size above 1° latitude. The lines-of-sight are sampled non-uniformly for $|b| \leq 1^\circ$ and with a fixed `db` for $|b| > 1^\circ$ up to `b_max`.
- `fractional_contribution`, `h`, `sigma_arm`, `arm_angles` and `pitch_angles` are the final parameters for this function, and are the parameters for the arms themselves as well as the density scale length `h` which enters Equation (11). By default, these values are set to those stored in `constants.py`, but could be set to different values when calling the function. `sigma_arm` corresponds to σ_A which enters Equation (10). `fractional_contribution`, `arm_angles` and `pitch_angles` have to contain the same number of values and could either be a Python list or a numpy array.

As briefly mentioned, `chi_squared.py` contains code which optimises the parameters entering the model. To run this script, one only has to call the function `run_tests(num_iterations=10)` and specify how many iterations you want the code to run. The default value is set to 10. For the first iteration, every parameter is varied around the value located in `constants.py`. The best parameters are kept and used as input in the next iteration. The best-fit parameters are printed to the terminal when the script is finished.

In `gum_cygnus.py`, we generate and save to file the intensities resulting from the modelled Cygnus X region and Gum Nebula. The calculations for both are done by calling the function `generate_gum_cygnus()`, which in turn calls the functions `gum()` and `cygnus()`. The latter functions calculate the Gum Nebula and the Cygnus X region, respectively, as described in the text. If the user wants to change the parameters for these regions, this can be done within `gum()` and `cygnus()`.

4.3. *galaxy_model*

The final folder contains the scripts simulating the OB associations. The first file, `galaxy_density_distr.py`, generates the coordinates for the Galaxy. The grid is generated in (x, y, z) coordinates with uniform spacing between each point. The generated coordinates and densities are saved to file and are generated by calling the function `generate_coords_densities()`. The parameters which enter this function are:

- `plane=1000`: This is the number of points along the x and y direction whose default value is 1000, such that the Galactic plane has a total of 10^6 number of points at which the OB associations can be placed.
- `transverse=20`: This is the number of points along the z direction whose default values is 20. As such, with the default value for `plane`, the number of grid points for which the OB associations could be placed is 20 million.
- `half_edge=40`: This is the distance in kpc from the Galactic center along the x and y axis for which the Galaxy is defined. The default value is set to 40 kpc, which is the distance from the Galactic center to the endpoint of the spiral arms 35 kpc plus 5 kpc to take into account the falloff in density transverse the spiral arms.
- `readfile_effective_area=True`: This boolean parameter does the same job as in `calc_modelled_intensity`. Set this to `False` the first time the code is run and anytime parameters for the modelled Galaxy are changed. Otherwise, set it to `True` to save time running the code.
- `read_data_from_file=True`: This boolean parameter, which defaults to `True`, controls whether or not the coordinates and densities are read from file or calculated. Set this parameter to `False` the first time the code is run to calculate coordinates and densities and save them to file. When it is set to `True`, coordinates and densities are read from file.

The code uses an object-oriented approach for modelling OB associations. We have three main classes: one for the Galaxy, one for the OB associations, and one for the OB stars. These are, respectively, located in the following files: `galaxy_class.py`, `association_class.py` and `supernovae_class.py`. The Galaxy class is mainly responsible for generating and storing the Galaxy's coordinates and densities, and drawing the positions of OB associations with a Monte Carlo simulation every Myr. When creating an instance of the Galaxy class, three parameters can be passed to it: `star_formation_episodes`, `sim_time_duration` and `read_data_from_file`. `sim_time_duration` is the number of Myr ago the simulation shall start. The Galaxy is generated in the past to produce SNe which could have produced cosmic rays observable today. Every Myr, we draw the association's placement from the emissivity map generated by `generate_coords_densities()`. The parameter `read_data_from_file` is passed on to `generate_coords_densities()`, and as mentioned, controls whether or not the coordinates and densities for the Galaxy are calculated or read from file.

The final parameter for the Galaxy class is `star_formation_episodes`, which controls how many star forming episodes shall occur in each association. Each episode is separated by 4 Myr and they are equal in size. Finally, the parameter α , which enters Eq. (13), can be changed using the `alpha` argument of the function `_association_distribution` located within the Galaxy class.

The Galaxy Class generates associations for every Myr by creating instances of the association class, which in turn creates instances of the supernovae class to store information about each OB star. If the user wants to modify the calculated age or the IMF used, this is done in `utilities.py`.

5. Summary

We have presented a model for the longitudinal profile of the NII intensity in the Galactic plane. The model is based on four logarithmic spiral arms, to which features like the Local Arm and local sources are

added. Since N II is a tracer of the line emission of OB associations, this model allows one to generate the spatial and temporal average distribution of OB associations and, thence, of core-collapse supernovae in the Milky Way. In addition to this average population, the model includes supernovae from known OB associations, providing thereby a more accurate description of the nearby Galaxy.

The complete model is made publicly available in the python code `SNOB`. The code can be used to generate the source distribution of Galactic CRs, and the distribution of birth places of pulsars or black holes. Moreover, accounting for H II regions might be useful in the interpretation of radio dispersion and scattering measurements as electron density tracers.

Acknowledgements

We would like to thank D.J. Fixsen for helpful advice on the FIRAS data and D. Semikoz for useful suggestions.

References

- [1] W. Baade, F. Zwicky, Cosmic Rays from Super-novae, *Proceedings of the National Academy of Science* 20 (1934) 259–263. doi:10.1073/pnas.20.5.259.
- [2] V. L. Ginzburg, S. I. Syrovatskii, *The origin of cosmic rays*, New York: Gordon and Breach, 1969.
- [3] A. M. Hillas, Can diffusive shock acceleration in supernova remnants account for high-energy galactic cosmic rays?, *J. Phys. G31* (2005) R95–R131. doi:10.1088/0954-3899/31/5/R02.
- [4] S. E. Woosley, T. A. Weaver, The Evolution and Explosion of Massive Stars. II. Explosive Hydrodynamics and Nucleosynthesis, *Astrophys. J. Suppl.* 101 (1995) 181. doi:10.1086/192237.
- [5] S. J. Smartt, Progenitors of Core-Collapse Supernovae, *Ann. Rev. Astron. Astrophys.* 47 (1) (2009) 63–106. arXiv:0908.0700, doi:10.1146/annurev-astro-082708-101737.
- [6] N. J. Shaviv, E. Nakar, T. Piran, Natural explanation for the anomalous positron to electron ratio with supernova remnants as the sole cosmic ray source, *Phys. Rev. Lett.* 103 (2009) 111302. arXiv:0902.0376, doi:10.1103/PhysRevLett.103.111302.
- [7] P. De La Torre Luque, T. Linden, Galactic Gas Models Strongly Affect the Determination of the Diffusive Halo Height arXiv:2408.05179.
- [8] D. A. Green, Constraints on the distribution of supernova remnants with Galactocentric radius, *Mon. Not. Roy. Astron. Soc.* 454 (2) (2015) 1517–1524. arXiv:1508.02931, doi:10.1093/mnras/stv1885.
- [9] S. Ranasinghe, D. Leahy, Distances, Radial Distribution, and Total Number of Galactic Supernova Remnants, *Astrophys. J.* 940 (1) (2022) 63. arXiv:2209.04570, doi:10.3847/1538-4357/ac940a.
- [10] J. T. Xie, J. B. Wang, N. Wang, R. Manchester, G. Hobbs, Modeling the Radial Distribution of Pulsars in the Galaxy, *Astrophys. J. Lett.* 963 (2) (2024) L39. arXiv:2402.11428, doi:10.3847/2041-8213/ad2850.
- [11] J. C. Higdon, R. E. Lingenfelter, OB Associations, Supernova-generated Superbubbles, and the Source of Cosmic Rays, *Astrophys. J.* 628 (2) (2005) 738–749. doi:10.1086/430814.
- [12] J. C. Higdon, R. E. Lingenfelter, The Galactic Spatial Distribution of OB Associations and their Surrounding Supernova-generated Superbubbles, *Astrophys. J.* 775 (2) (2013) 110. arXiv:1302.1223, doi:10.1088/0004-637X/775/2/110.
- [13] S. K. Ocker, L. D. Anderson, T. J. W. Lazio, J. M. Cordes, V. Ravi, Implications for Galactic Electron Density Structure from Pulsar Sightlines Intersecting H II Regions arXiv:2406.07664.
- [14] D. J. Fixsen, C. L. Bennett, J. C. Mather, COBE Far Infrared Absolute Spectrophotometer Observations of Galactic Lines, *Astrophys. J.* 526 (1) (1999) 207–214. doi:10.1086/307962.
- [15] D. Fixsen, private communication.
- [16] GRAVITY Collaboration, R. Abuter, et al., A geometric distance measurement to the Galactic center black hole with 0.3% uncertainty, *Astron. Astrophys.* 625 (2019) L10. arXiv:1904.05721, doi:10.1051/0004-6361/201935656.
- [17] K. R. Anantharamaiah, On the origin of the Galactic ridge recombination lines, *Journal of Astrophysics and Astronomy* 7 (1986) 131–139. doi:10.1007/BF02714206.
- [18] D. A. Roshi, K. R. Anantharamaiah, Hydrogen Recombination Lines near 327 MHz. III. Physical Properties and Origin of the Low-Density Ionized Gas in the Inner Galaxy, *Astrophys. J.* 557 (1) (2001) 226–239. doi:10.1086/321586.
- [19] C. Quireza, R. T. Rood, D. S. Balser, T. M. Bania, Radio Recombination Lines in Galactic H II Regions, *Astrophys. J. Suppl.* 165 (1) (2006) 338–359. arXiv:astro-ph/0603133, doi:10.1086/503901.
- [20] B. C. Reed, New Estimates of the Scale Height and Surface Density of OB Stars in the Solar Neighborhood, *Astron. J.* 120 (1) (2000) 314–318. doi:10.1086/301421.
- [21] A. A. Stark, Y. Lee, The Scale Height of Giant Molecular Clouds Is Less than That of Smaller Clouds, *Astrophys. J. Lett.* 619 (2) (2005) L159–L162. arXiv:astro-ph/0403631, doi:10.1086/427936.
- [22] C. F. McKee, J. P. Williams, The Luminosity Function of OB Associations in the Galaxy, *Astrophys. J.* 476 (1) (1997) 144–165. doi:10.1086/303587.
- [23] L. F. Smith, P. Biermann, P. G. Mezger, Star formation rates in the Galaxy., *Astron. Astrophys.* 66 (1978) 65–76.
- [24] C. Esteban, J. García-Rojas, Revisiting the radial abundance gradients of nitrogen and oxygen of the Milky Way, *Mon. Not. Roy. Astron. Soc.* 478 (2) (2018) 2315–2336. arXiv:1805.00714, doi:10.1093/mnras/sty1168.

- [25] Y. M. Geogelin, Y. P. Geogelin, The spiral structure of our Galaxy determined from H II regions., *Astron. Astrophys.* 49 (1976) 57–79.
- [26] J. P. Vallée, New Velocimetry and Revised Cartography of the Spiral Arms in the Milky Way—A Consistent Symbiosis, *Astron. J.* 135 (4) (2008) 1301–1310. doi:10.1088/0004-6256/135/4/1301.
- [27] J. P. Vallée, A Synthesis of Fundamental Parameters of Spiral Arms, Based on Recent Observations in the Milky Way, *International Journal of Astronomy and Astrophysics* 3 (1) (2013) 20–28. doi:10.4236/ijaa.2013.31003.
- [28] L. G. Hou, J. L. Han, The observed spiral structure of the Milky Way, *Astron. Astrophys.* 569 (2014) A125. arXiv:1407.7331, doi:10.1051/0004-6361/201424039.
- [29] T. Y. Steiman-Cameron, M. Wolfire, D. Hollenbach, COBE and the Galactic Interstellar Medium: Geometry of the Spiral Arms from FIR Cooling Lines, *Astrophys. J.* 722 (2) (2010) 1460–1473. doi:10.1088/0004-637X/722/2/1460.
- [30] J. H. Taylor, J. M. Cordes, Pulsar Distances and the Galactic Distribution of Free Electrons, *Astrophys. J.* 411 (1993) 674. doi:10.1086/172870.
- [31] J. M. Cordes, T. J. W. Lazio, NE2001.I. A New Model for the Galactic Distribution of Free Electrons and its Fluctuations, arXiv:astro-ph/0207156.
- [32] R. Drimmel, D. N. Spergel, Three-dimensional Structure of the Milky Way Disk: The Distribution of Stars and Dust beyond $0.35 R_{\text{solar}}$, *Astrophys. J.* 556 (1) (2001) 181–202. arXiv:astro-ph/0101259, doi:10.1086/321556.
- [33] Benjamin, et al., First GLIMPSE Results on the Stellar Structure of the Galaxy, *Astrophys. J. Lett.* 630 (2) (2005) L149–L152. arXiv:astro-ph/0508325, doi:10.1086/491785.
- [34] R. A. Benjamin, The Spiral Structure of the Galaxy: Something Old, Something New..., in: H. Beuther, H. Linz, T. Henning (Eds.), *Massive Star Formation: Observations Confront Theory*, Vol. 387 of *Astronomical Society of the Pacific Conference Series*, 2008, p. 375.
- [35] L. G. Hou, J. L. Han, Offset between stellar spiral arms and gas arms of the Milky Way, *Mon. Not. Roy. Astron. Soc.* 454 (1) (2015) 626–636. arXiv:1508.04263, doi:10.1093/mnras/stv1904.
- [36] A. L. Quintana, N. J. Wright, Revisiting the Cygnus OB associations, *Mon. Not. Roy. Astron. Soc.* 508 (2) (2021) 2370–2385. arXiv:2109.07499, doi:10.1093/mnras/stab2663.
- [37] N. J. Wright, OB Associations and their origins, *New Astron. Rev.* 90 (2020) 101549. arXiv:2011.09483, doi:10.1016/j.newar.2020.101549.
- [38] N. J. Wright, J. E. Drew, M. Mohr-Smith, The massive star population of Cygnus OB2, *Mon. Not. Roy. Astron. Soc.* 449 (1) (2015) 741–760. arXiv:1502.05718, doi:10.1093/mnras/stv323.
- [39] K. L. J. Rygl, A. Brunthaler, A. Sanna, K. M. Menten, M. J. Reid, H. J. van Langevelde, M. Honma, K. J. E. Torstensson, K. Fujisawa, Parallaxes and proper motions of interstellar masers toward the Cygnus X star-forming complex. I. Membership of the Cygnus X region, *Astron. Astrophys.* 539 (2012) A79. arXiv:1111.7023, doi:10.1051/0004-6361/201118211.
- [40] B. Reipurth, N. Schneider, Star Formation and Young Clusters in Cygnus, in: B. Reipurth (Ed.), *Handbook of Star Forming Regions*, Volume I, Vol. 4, 2008, p. 36.
- [41] C. S. Gum, A large H II region at galactic longitude 226 deg., *The Observatory* 72 (1952) 151–154.
- [42] R. J. Reynolds, Observations of the Gum nebula with a Fabry-Perot spectrometer., *Astrophys. J.* 203 (1976) 151–153. doi:10.1086/154057.
- [43] J. Maíz-Apellániz, N. R. Walborn, H. Á. Galué, L. H. Wei, A Galactic O Star Catalog, *Astrophys. J. Suppl.* 151 (1) (2004) 103–148. arXiv:astro-ph/0311196, doi:10.1086/381380.
- [44] F. Millour, et al., Direct constraint on the distance of γ^2 Velorum from AMBER/VLTI observations, *Astron. Astrophys.* 464 (1) (2007) 107–118. arXiv:astro-ph/0610936, doi:10.1051/0004-6361:20065408.
- [45] D. Forbes, Optical spiral structure between $L = 30$ deg and 70 deg, in: W. L. H. Shuter (Ed.), *Kinematics, Dynamics and Structure of the Milky Way*, Vol. 100 of *Astrophysics and Space Science Library*, 1983, pp. 217–222.
- [46] D. Forbes, Optical spiral structure at $L = 30$ to 70 . I. New observations of distant early-type stars., *Astron. J.* 89 (1984) 475–479. doi:10.1086/113537.
- [47] D. Forbes, Optical spiral structure at $L = 30$ - 70 deg. II - The distribution of interstellar extinction, *Astron. J.* 90 (1985) 301–307. doi:10.1086/113730.
- [48] G. A. Tammann, W. Loeffler, A. Schroeder, The Galactic Supernova Rate, *Astrophys. J. Suppl.* 92 (1994) 487. doi:10.1086/192002.
- [49] S. van den Bergh, R. D. McClure, Rediscussion of Extragalactic Supernova Rates Derived from Evans’s 1980–1988 Observations, *Astrophys. J.* 425 (1994) 205. doi:10.1086/173975.
- [50] P. Kroupa, The Initial Mass Function of Stars: Evidence for Uniformity in Variable Systems, *Science* 295 (5552) (2002) 82–91. arXiv:astro-ph/0201098, doi:10.1126/science.1067524.
- [51] J. Kennicutt, Robert C., B. K. Edgar, P. W. Hodge, Properties of H II Region Populations in Galaxies. II. The H II Region Luminosity Function, *Astrophys. J.* 337 (1989) 761. doi:10.1086/167147.
- [52] M.-M. Mac Low, R. McCray, Superbubbles in Disk Galaxies, *Astrophys. J.* 324 (1988) 776. doi:10.1086/165936.
- [53] C. Heiles, Clustered Supernovae versus the Gaseous Disk and Halo, *Astrophys. J.* 354 (1990) 483. doi:10.1086/168709.
- [54] K. M. Ferriere, The Hot Gas Filling Factor in the Vicinity of the Sun, *Astrophys. J.* 441 (1995) 281. doi:10.1086/175355.
- [55] B. G. Elmegreen, C. J. Lada, Sequential formation of subgroups in OB associations., *Astrophys. J.* 214 (1977) 725–741. doi:10.1086/155302.
- [56] G. Schaller, D. Schaerer, G. Meynet, A. Maeder, New Grids of Stellar Models from 0.8-SOLAR-MASS to 120-SOLAR-MASSSES at $Z=0.020$ and $Z=0.001$, *Astron. Astrophys. Suppl.* 96 (1992) 269.
- [57] B. Fuchs, D. Breitschwerdt, M. A. de Avillez, C. Dettbarn, C. Flynn, The search for the origin of the Local Bubble redivivus, *Mon. Not. Roy. Astron. Soc.* 373 (3) (2006) 993–1003. arXiv:astro-ph/0609227, doi:10.1111/j.1365-2966.2006.11044.x.
- [58] V. Mikalsen, Modelling the Galactic NII intensities and the distribution of OB associations, Master’s thesis, NTNU

- Trondheim, available at <https://hdl.handle.net/11250/3143779> (2024).
- [59] M. J. Pecaut, E. E. Mamajek, Intrinsic Colors, Temperatures, and Bolometric Corrections of Pre-main-sequence Stars, *Astrophys. J. Suppl.* 208 (1) (2013) 9. arXiv:1307.2657, doi:10.1088/0067-0049/208/1/9.
- [60] E. Mamajek, A modern mean dwarf stellar color and effective temperature sequence, http://www.pas.rochester.edu/~emamajek/EEM_dwarf_UBVIJHK_colors_Teff.txt, version 2022.04.16, accessed on 2024-02-08 (04 2022).